The Astrophysical Journal, 893:16 (12pp), 2020 April 10 https://doi.org/10.3847/1538-4357/ab7999

Constraints on the Emission of Gamma-Rays from M31 with HAWC

A. Albert[1], R. Alfaro[2], C. Alvarez[3], J. C. Arteaga-Velázquez[4], K. P. Arunbabu[5], D. Avila Rojas[2], H. A. Ayala Solares[6], E. Belmont-Moreno[2], S. Y. BenZvi[7], C. Brisbois[8], K. S. Caballero-Mora[3], T. Capistrán[9], A. Carramiñana[9], S. Casanova[10], U. Cotti[4], J. Cotzomi[11], S. Coutiño de León[9], E. De la Fuente[12], C. de León[4], S. Dichiara[13], B. L. Dingus[1], M. A. DuVernois[14], K. Engel[15], C. Espinoza[2], H. Fleischhack[8], N. Fraija[13], A. Galván-Gámez[13], D. García-Aguilar[2], J. A. García-González[2], F. Garfias[13], M. M. González[13], J. A. Goodman[15], J. P. Harding[1], S. Hernandez[2], B. Hona[8], D. Huang[8], F. Hueyotl-Zahuantitla[3], P. Hüntemeyer[8], A. Iriarte[13], A. Jardin-Blicq[16], V. Joshi[16], D. Kieda[17], W. H. Lee[13], H. León Vargas[2], A. L. Longinotti[9], G. Luis-Raya[18], K. Malone[1], S. S. Marinelli[19], O. Martinez[11], I. Martinez-Castellanos[15], J. Martínez-Castro[20], J. A. Matthews[21], P. Miranda-Romagnoli[22], J. A. Morales-Soto[4], E. Moreno[11], M. Mostafá[6], A. Nayerhoda[10], L. Nellen[23], M. Newbold[17], R. Noriega-Papaqui[22], A. Peisker[19], E. G. Pérez-Pérez[18], Z. Ren[21], C. D. Rho[7,26], D. Rosa-González[9], M. Rosenberg[6], R. Rubenzahl[24], H. Salazar[11], F. Salesa Greus[10], A. Sandoval[2], M. Schneider[15], G. Sinnis[1], A. J. Smith[15], R. W. Springer[17], P. Surajbali[16], E. Tabachnick[15], O. Tibolla[18], K. Tollefson[19], I. Torres[9], L. Villaseñor[11], J. Wood[14], T. Yapici[7], A. Zepeda[25], and H. Zhou[1]

[1] Physics Division, Los Alamos National Laboratory, Los Alamos, NM, USA
[2] Instituto de Física, Universidad Nacional Autónoma de México, Mexico City, Mexico
[3] Universidad Autónoma de Chiapas, Tuxtla Gutiérrez, Chiapas, Mexico
[4] Universidad Michoacana de San Nicolás de Hidalgo, Morelia, Mexico
[5] Instituto de Geofísica, Universidad Nacional Autónoma de México, Mexico City, Mexico
[6] Department of Physics, Pennsylvania State University, University Park, PA, USA
[7] Department of Physics & Astronomy, University of Rochester, Rochester, NY, USA; tyapici@ur.rochester.edu, crho2@ur.rochester.edu, cdr397@skku.edu
[8] Department of Physics, Michigan Technological University, Houghton, MI, USA
[9] Instituto Nacional de Astrofísica, Óptica y Electrónica, Puebla, Mexico
[10] Institute of Nuclear Physics Polish Academy of Sciences, PL-31342 IFJ-PAN, Krakow, Poland
[11] Facultad de Ciencias Físico Matemáticas, Benemérita Universidad Autónoma de Puebla, Puebla, Mexico
[12] Departamento de Física, Centro Universitario de Ciencias Exactase Ingenierias, Universidad de Guadalajara, Guadalajara, Mexico
[13] Instituto de Astronomía, Universidad Nacional Autónoma de México, Mexico City, Mexico
[14] Department of Physics, University of Wisconsin-Madison, Madison, WI, USA
[15] Department of Physics, University of Maryland, College Park, MD, USA
[16] Max-Planck Institute for Nuclear Physics, D-69117 Heidelberg, Germany
[17] Department of Physics and Astronomy, University of Utah, Salt Lake City, UT, USA
[18] Universidad Politecnica de Pachuca, Pachuca, Hidalgo, Mexico
[19] Department of Physics and Astronomy, Michigan State University, East Lansing, MI, USA
[20] Centro de Investigación en Computación, Instituto Politécnico Nacional, Mexico City, Mexico
[21] Dept of Physics and Astronomy, University of New Mexico, Albuquerque, NM, USA
[22] Universidad Autónoma del Estado de Hidalgo, Pachuca, Mexico
[23] Instituto de Ciencias Nucleares, Universidad Nacional Autónoma de Mexico, Mexico City, Mexico
[24] Department of Astronomy, California Institute of Technology, Pasadena, CA, USA
[25] Physics Department, Centro de Investigacion y de Estudios Avanzados del IPN, Mexico City, Mexico
Received 2020 January 6; revised 2020 February 22; accepted 2020 February 23; published 2020 April 8

Abstract

Cosmic rays, along with stellar radiation and magnetic fields, are known to make up a significant fraction of the energy density of galaxies such as the Milky Way. When cosmic rays interact in the interstellar medium, they produce gamma-ray emission which provides an important indication of how the cosmic rays propagate. Gamma-rays from the Andromeda galaxy (M31), located 785 kpc away, provide a unique opportunity to study cosmic-ray acceleration and diffusion in a galaxy with a structure and evolution very similar to the Milky Way. Using 33 months of data from the High Altitude Water Cherenkov Observatory, we search for teraelectronvolt gamma-rays from the galactic plane of M31. We also investigate past and present evidence of galactic activity in M31 by searching for Fermi bubble-like structures above and below the galactic nucleus. No significant gamma-ray emission is observed, so we use the null result to compute upper limits on the energy density of cosmic rays >10 TeV in M31.

Unified Astronomy Thesaurus concepts: High energy astrophysics (739); Particle astrophysics (96); Galactic cosmic rays (567); Gamma-ray astronomy (628); Andromeda Galaxy (39)

1. Introduction

The study of the properties of the Milky Way is unique in that it provides the opportunity to observe the features of the Galaxy from within, but at the same time it is challenging to obtain a global perspective of Galactic properties. Messier 31 (M31), also called the Andromeda galaxy, is the closest neighboring major galaxy to the Milky Way and it is known to be a spiral galaxy of similar structure to the Milky Way. Moreover, M31 is one of the seven external star-forming galaxies that have been observed in gigaelectronvolt gamma-rays (Abdo et al. 2010; Ackermann et al. 2017). M31 also

[26] Now at Natural Science Research Institute, University of Seoul, Seoul, Republic of Korea.

differs from the Milky Way in important ways: for example, its total stellar mass is a factor of 1.1 to 2 larger than our own Galaxy (Yin et al. 2009; Sick et al. 2014; Licquia & Newman 2015), while its star formation rate (SFR) is a factor of 2 to 5 lower (Yin et al. 2009; Azimlu et al. 2011; Licquia & Newman 2015), possibly decreasing from a peak in the past 10 to 100 Myr (Kang et al. 2009). The similarities and differences make M31 an excellent complement for the study of astrophysics in the Milky Way.

In galaxies such as the Milky Way and M31, cosmic rays can have energy densities comparable to the contributions from magnetic fields and radiation (Garmire & Kraushaar 1965). Thus, they are likely to have a significant influence on galactic dynamics. Moreover, cosmic rays are potential probes of other poorly understood galactic properties such as the SFR. Due to the presence of Galactic and extragalactic magnetic fields, it is not possible to directly associate charged cosmic rays measured at Earth with acceleration sites in the Milky Way or in other galaxies such as M31. However, cosmic-ray interactions with radiation and dense material near their production sites can produce high-energy photons, allowing us to probe particle acceleration indirectly. Charged particle acceleration can easily produce spectrally "hard" gamma-ray emission extending to teraelectronvolt energies (Dwek & Krennrich 2013). The gamma-ray flux from a galaxy provides an indirect measurement of the energy density of cosmic rays in the galaxy. With sufficient data, this measurement can then be used to estimate the SFR.

For example, the *Fermi* Large Area Telescope (*Fermi* LAT) has detected a $\sim 10\sigma$ excess of gigaelectronvolt gamma-rays with a spectral index of Γ of -2.4 ± 0.1 from the core of M31, and they found agreement between the observed gamma-ray energy flux (Ackermann et al. 2017) and the calculated SFR of 0.35–1.0 $M_\odot\,\mathrm{yr}^{-1}$ by Yin et al. (2009). M31 has also been studied for its cosmic-ray energy density and other properties by Yoast-Hull et al. (2016). Recently, the Milky Way was found to have undergone past periods of Galactic activity via the discovery of the "*Fermi* Bubbles" (FBs; Su et al. 2010; Ackermann et al. 2014). The FBs were first detected during a search for residual gamma-rays between 1–100 GeV measured by the *Fermi* LAT (Su et al. 2010). The bubbles subtend approximately 0.8 sr above and below the Galactic Center and are located 9.4 kpc from the Sun under the assumption that they originate from the Galactic Center (Ackermann et al. 2014). Since most spiral galaxies are believed to contain supermassive black holes at their centers, they may also undergo periods of high activity that give rise to bubble-like structures. Therefore, in the very high energy (VHE) gamma-ray analysis of M31 presented in this paper, we take into consideration the possibility that M31 has its own set of FBs. We assume a simple morphological model in our analysis based on a study of data from the *Fermi* LAT by Pshirkov et al. (2016), which indicated that M31 does contain two 6–7.5 kpc circular regions of gamma-ray emission between 0.1–300 GeV. We note that this emission was not reported in a subsequent publication by the *Fermi* LAT Collaboration (Ackermann et al. 2017).

At teraelectronvolt energies, the *VERITAS* Collaboration collected data from several regions around M31 for 54 hr, searching for evidence of VHE emission from the M31 galactic plane and the bubble regions (Bird 2016). However, no significant emission was observed. *VERITAS* has excellent energy and angular resolution and is very sensitive to point sources, but M31 is a spatially extended source covering roughly $3.^\circ 2 \times 1^\circ$ (Bird 2016), making observations with *VERITAS* difficult. On the other hand, the High Altitude Water Cherenkov (HAWC) observatory is well suited to perform unbiased measurements of gamma-rays from spatially extended objects. HAWC is conducting a survey of 2/3 of the sky in gamma-rays and is sensitive to gamma-rays with energies ranging from 1 TeV to a few hundred TeV (Abeysekara et al. 2017a, 2017b, 2019). HAWC is located at 4100 m above sea level, at a latitude of $18^\circ 59.'7$ N and longitude of $97^\circ 18.'6$ W. The nucleus of M31 is located at $\alpha_{J2000} = 0^\mathrm{h}\,43^\mathrm{m}\,35.^\mathrm{s}43$, $\delta_{J2000} = +41^\circ\,20'56.''8$, and the galaxy transits 22° from the zenith of the HAWC detector.

In this paper, we present a systematic search of the extended gamma-ray emission from M31's disk and its possible bubble-like regions above 1 TeV using 33 months of data from HAWC. The paper is structured as follows. We present the spatial models of M31, its possible associated bubbles, and analysis method in Section 2; in Section 3 we provide gamma-ray upper limits for M31, the bubbles and the combined morphology. We also constrain the cosmic-ray energy density in the M31 disk in Section 3.

2. Method

The analysis of gamma-ray sources with HAWC is described in detail in Abeysekara et al. (2017a). In brief, the energy of each gamma-ray is estimated from the fraction of the optical sensors in HAWC triggered by gamma-ray air showers. To estimate the energy spectrum of an observed source of gamma-rays, parametric spatial and spectral models of gamma-ray sources are fitted to HAWC data using a maximum-likelihood technique. We employ the Multi-Mission Maximum Likelihood analysis framework (Vianello et al. 2015; Younk et al. 2015) to fit parametric spatial and spectral models to the HAWC data. For both the M31 disk and bubble regions, we assume the gamma-ray emission is described by a simple power law

$$\frac{dN}{dE} = K\left(\frac{E}{E_0}\right)^{\Gamma}, \tag{1}$$

where K is a normalization constant, E_0 is the pivot energy, and Γ is the spectral index. For the disk-only analysis, we perform a maximum-likelihood fit of the flux normalization with three different fixed spectral indices. The same procedure is followed for the bubbles-only analysis. For the combined case, we perform the analysis for all combinations of spectral indices for the disk and the bubble regions. Note that when fitting, the normalizations and the spectral indices are assumed to be same for both bubbles. Throughout the analysis, a fixed pivot energy of $E_0 = 1$ TeV is used and the spectral indices of $[-2.0, -2.5, -3.0]$ are considered. Our estimate of statistical significance, the "test statistic" (TS), is computed for each fit as follows (Wilks 1938; Albert et al. 2018):

$$\mathrm{TS} = 2\ln\frac{\mathcal{L}(\text{source(s)} + \text{background})}{\mathcal{L}(\text{background})} \tag{2}$$

$$\text{significance} \approx \sqrt{\mathrm{TS}}\ [\text{Gaussian } \sigma]. \tag{3}$$

The maximum-likelihood estimators are used to find the best normalizations, $\hat{K}_{\mathrm{disk}}$ and $\hat{K}_{\mathrm{FB}}$. We then use $\hat{K}_{\mathrm{disk}}$ and $\hat{K}_{\mathrm{FB}}$ as

Table 1
Definition of Energy Bins Used for the Quasi-differential Limit Calculations, Following the Analysis Used in Aartsen et al. (2017)

Energy bin	Lower Energy (TeV)	Higher Energy (TeV)	Pivot Energy (E_0) (TeV)
1	0.56	1.78	1.0
2	1.78	5.62	3.16
3	5.62	17.78	10.0
4	17.78	56.23	31.63
5	56.23	177.8	100.0

Table 2
Positions of M31 Regions from the IRIS Database (Miville-Deschenes & Lagache 2005; Pshirkov et al. 2016)

Region	α_{J2000}	δ_{J2000}
M31 nucleus	10.°6848	41.°7166
M31 disk endpoint 1	11.°1509	40.°8256
M31 disk endpoint 2	10.°2145	40.°8256
FB1 center	10.°3746	41.°5951
FB2 center	10.°9949	40.°9430

Note. The two endpoints and nucleus of M31 define the galactic plane, which we use to locate two positions perpendicular and symmetric to the center of the plane (FB1 and FB2) that are spaced 0.°45 from the nucleus.

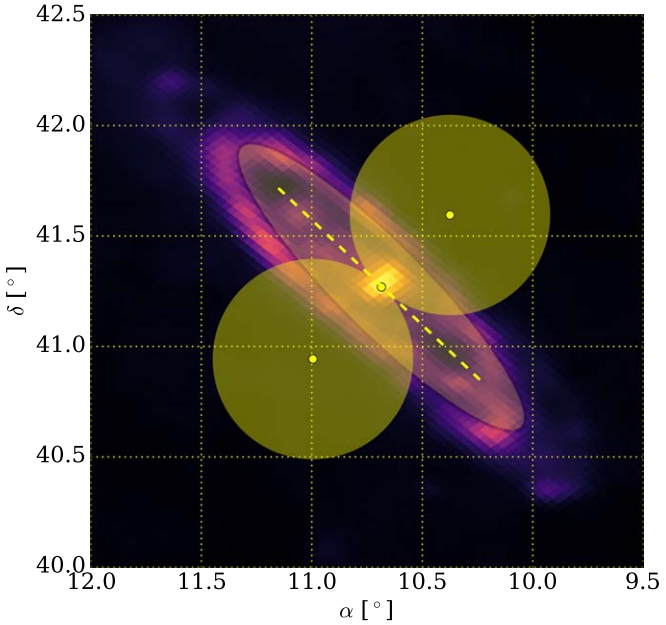

Figure 1. Regions to be used in the model for the FBs around M31. The M31 galactic plane is modeled as an ellipse with the two FBs as circular regions with radius 0.°45. The background image is the IRIS 100 μm map of the 2.°5 × 2.°5 region surrounding M31. The dashed line represents the M31 galactic plane between the two endpoints defined in Table 2.

input to a Markov-Chain Monte Carlo (MCMC) in order to estimate the distribution of the posterior likelihood around the maximum. In the MCMC, a uniform prior range is assumed for both $K_{\rm disk}$ and $K_{\rm FB}$ between 0 and 10^{-11} TeV^{-1} cm^{-2} s^{-1}. Given the lack of statistically significant VHE emission, the MCMC results are then used to compute 95% credible upper intervals on the flux normalization.

In addition to upper limits on K assuming a fixed Γ for the disk, bubbles, and disk and bubbles in combination, we also compute quasi-differential limits between 1–100 TeV. That is, the data are sorted into five energy bins $j \in [1,\ldots,5]$ and independent power-law fits are used to constrain K_j and Γ_j in each bin. The bin widths correspond to a half-decade in gamma-ray energy, following the analysis of HAWC data presented in Aartsen et al. (2017), with the pivot energy $E_{0,j}$ set to the center of the logarithmic energy range of bin j. The energy bins are defined in Table 1.

2.1. Model Templates

We treat the morphology of the M31 FBs as described in Pshirkov et al. (2016). The position of the core of M31 is taken from the 100 μm infrared map found in the Improved Reprocessing of the *IRAS* Survey (IRIS) database (Miville-Deschenes & Lagache 2005). The location of the M31 galactic center, the positions of the bubbles, and the orientation of the disk of M31 used in the analysis are given in Table 2.

The M31 galactic disk is modeled as an ellipse with a semimajor axis of length 0.°9 inclined 45.°04 counterclockwise from the positive R.A. axis. The ellipse has an aspect ratio of $b/a = 0.22$ (Pshirkov et al. 2016). The two FB regions are modeled as circular disks of radius 0.°45, oriented perpendicular to and symmetrically above and below the galactic plane of M31. Figure 1 displays the regions used in the spatial fit. Two of the model templates used in the analysis are based on M31 and the FB separately. The third model template is the combination of M31 and the FBs. The flux is assumed to be constant within the area encompassed by the template.

2.2. Cosmic-Ray Energy Density

Using a measurement of or constraint on the flux of teraelectronvolt gamma-rays, under the assumption that gamma-ray emission is due to the decay of neutral pions produced by cosmic-ray interactions, the energy density of cosmic rays responsible for the production of gamma-rays can be derived using (Abramowski et al. 2016)

$$\omega_{\rm CR}(\geqslant 10E_\gamma) \sim 1.8 \times 10^{-2}\left(\frac{\eta_n}{1.5}\right)^{-1} \times \left(\frac{L_\gamma(\geqslant E_\gamma)}{10^{34}\ {\rm erg\ s^{-1}}}\right)\left(\frac{M}{10^6\ M_\odot}\right)^{-1} {\rm eV\ cm^{-3}}. \quad (4)$$

In Equation (4), $L_\gamma(\geqslant E_\gamma)$ is the observed gamma-ray luminosity at energies beyond E_γ, and M is the mass of target nuclei within the region of interest. Note that $\omega_{\rm CR}$ is estimated for $\geqslant 10E_\gamma$ because, on average, approximately 10% of the primary cosmic-ray energy goes into the production of gamma-ray photons via the interactions $pp \rightarrow pp\pi^0$ and $\pi^0 \rightarrow \gamma\gamma$. Estimates of target mass are typically based on measurements of H I and H_2; the quantity η_n is a scale factor fixed at 1.5 to account for nucleons present other than hydrogen (Abramowski et al. 2016). Since physical properties such as the mass of the galaxy are required for the calculation, the cosmic-ray energy density is only computed for M31 and not for the bubbles. In addition, we also compute the cosmic-ray energy density corresponding to a gamma-ray energy above 1 TeV for each energy bin adopted from the quasi-differential limits.

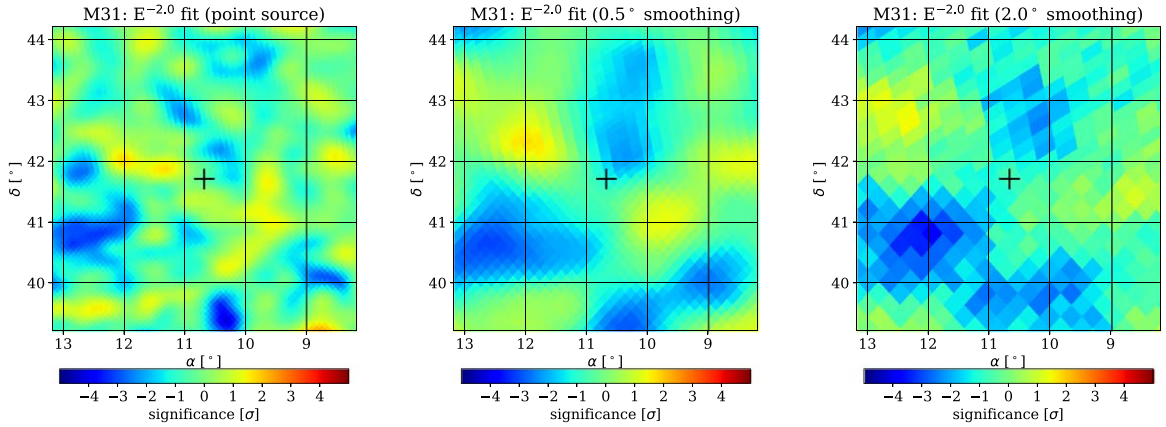

Figure 2. Significance map around M31 (crosshairs) produced with 33 months of HAWC data using (left) the point source map, (center) 0.°5-smoothed map and (right) 2°-smoothed map. An E^{-2} spectrum is used for the three maps.

Table 3
The Mass Budget Used to Calculate the Cosmic-Ray Energy Distribution

Mass H I	$(7.33 \pm 2.20) \times 10^9\, M_\odot$	Braun et al. (2009)
Mass H_2	$(3.45 \pm 1.80) \times 10^9\, M_\odot$	Nieten et al. (2006)
Distance	$d = 785 \pm 25$ kpc	McConnachie et al. (2005)
Flux uncertainty	±50%	Abeysekara et al. (2017a)

Current best estimates of the properties of M31 are used with relevant uncertainties (see Table 3). The uncertainties are propagated to calculate the systematic uncertainties on each value of ω_{CR}. Most of the uncertainties on the energy densities come from the estimates of the target mass and the detector systematics in the HAWC analysis (Abeysekara et al. 2017a).

3. Results

The analysis uses data recorded with HAWC between 2015 June and 2017 December (Abeysekara et al. 2017a). A description of the construction of HAWC sky maps is provided in Abeysekara et al. (2017b). In brief, maps of the sky around M31 are produced by binning the arrival directions of cosmic rays and gamma-rays in a HEALPix map (Gorski et al. 2005) using bins of width 0.°057, considerably smaller than the 0.°2 to 1° angular resolution of HAWC. Cosmic-ray air showers are identified and rejected based on the variance of the distribution of charge deposited as a function of distance from the reconstructed shower core. The rejection power of the cosmic-ray cut depends strongly on the size of the air shower; 10% of cosmic rays below 1 TeV pass the event selection, while 0.1% pass at 10 TeV (Abeysekara et al. 2017a). The gamma-ray selection efficiency is >30% at all energies.

Once the HEALPix map is filled, we produce a background map giving the expected number of counts from an isotropic distribution of events. The background expectation is computed from the data themselves using the direct integration method developed in Atkins et al. (2003). A maximum-likelihood technique is then used to search for significant excesses and deficits with respect to the isotropic background expectation as a function of sky location. The signal model in the likelihood assumes each HEALPix pixel includes background counts plus a flux from a power-law energy spectrum. The source or sources contributing to counts in a given pixel can be treated as point-like or spatially extended, assuming a uniform disk of fixed radius; the source morphology is convolved with the detector angular resolution in the likelihood.

Figure 2 shows HAWC sky maps around M31 assuming an E^{-2} source spectrum and a point-like source morphology (left), a source extended by 0.°5 (center), and a 2° extended source (right). The maps include all energies >1 TeV, and no significant excess emission is observed. Thus, for each of our model templates, we report 95% credible upper limits on the flux of gamma-rays above 1 TeV.

To estimate the sensitivity of our analysis, we calculate the expected upper limits of HAWC to the M31 disk and two FBs (as well as individual components of such a combined model) by fitting the same M31 spatial templates to background-only regions at different right ascensions, keeping the decl. of the templates fixed. By avoiding regions with known VHE gamma-ray sources, this produces a distribution of background-only estimates for the particular morphological models we are using. These are used to provide expected limits of the model templates used in our analysis and 68% and 95% containment bands of the expected limits.

3.1. Expected Gamma-Ray Flux from M31 FBs, Assuming Milky Way-like Emission

The observed spectral energy distribution (SED) of the Milky Way FBs reported by Ackermann et al. (2014) is approximately constant in the 1–100 GeV energy range. However, at higher energies the spectrum falls off as shown in Figure 3.

From the observed flux of the Milky Way bubbles, we can calculate the gamma-ray flux of equivalent bubble-like structures of M31, given the distance $d_{M31} = 785$ kpc between M31 and the Milky Way. This follows a similar analysis carried out by Pshirkov et al. (2016). Since HAWC is sensitive to gamma-rays in the teraelectronvolt regime, we extrapolate the SED to energies greater than 1 TeV. First, we calculate the integral flux of the Milky Way FBs by integrating the best-fit power law (dashed line in Figure 3) above 1 TeV multiplied by the total solid angle of the bubbles. To extrapolate the flux to what is expected from a similarly-sized source at the position of M31, we scale the integral flux by $(d_{MW}/d_{M31})^2$ where d_{MW} is the assumed distance to the Milky Way FBs. Under these assumptions, the expected integral flux from M31 FBs is approximately 3.9×10^{-15} cm^{-2} s^{-1} at energies >1 TeV.

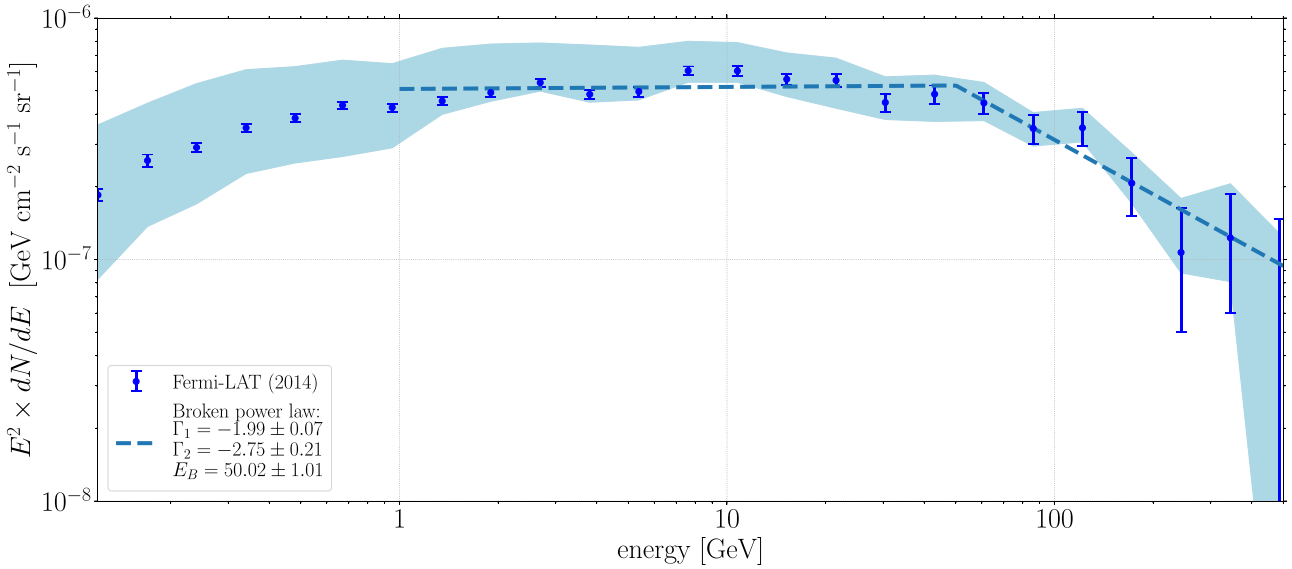

Figure 3. Spectral energy distribution (SED) of the Milky Way FBs, with statistical uncertainties shown as error bars and systematic uncertainties as the filled contour (Ackermann et al. 2014). The dashed line is a best-fit broken power law between 1–500 GeV with spectral indices Γ_1, Γ_2, and break energy E_B. Below 50 GeV the flux is an E^{-2} spectrum; above the spectrum is described by $E^{-2.75}$.

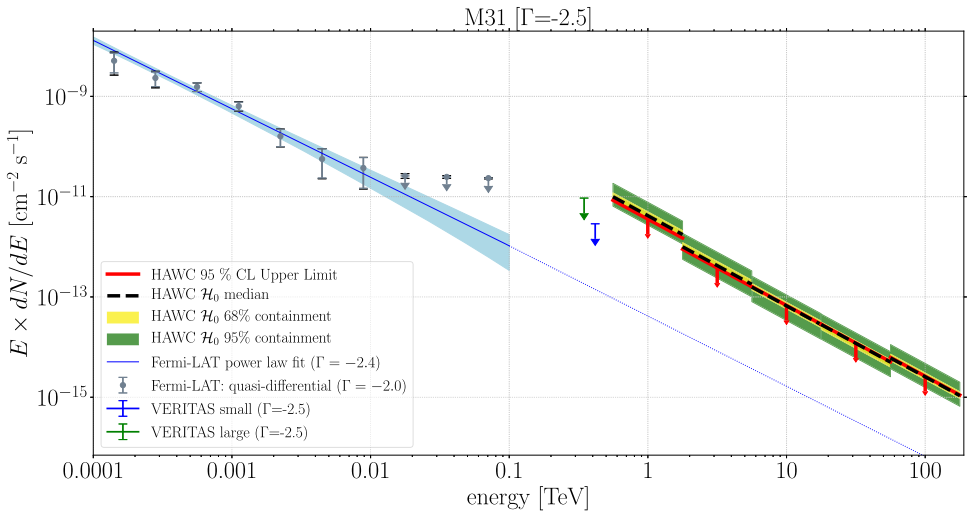

Figure 4. 95% credible upper intervals on gamma-ray emission from the disk of M31 using the 33 month data set from HAWC (red arrows), assuming an $E^{-2.5}$ power law. The expected range of upper limits assuming the null hypothesis of no emission ($\mathcal{H}_0$) was computed using background-only regions. For each quasi-differential energy bin, dotted lines represent mean upper limits, yellow boxes represent 68% containment regions for the upper limits, and green boxes represent 95% containment regions. (See Section 3 for details.) Also shown are measurements of M31 from *Fermi* LAT (Ackermann et al. 2017) and upper limits from *VERITAS* (Bird 2016).

Using the constant flux from 1 to 50 GeV (the dashed curve in Figure 3), we calculate the total integral flux expected from M31 bubbles to be 2.06×10^{-10} cm^{-2} s^{-1}. This is significantly below the integral flux of $(2.6 \pm 0.6) \times 10^{-9}$ cm^{-2} s^{-1} one obtains using the spectral index $\Gamma_{\rm FB} = 2.3 \pm 0.1$ reported by Pshirkov et al. (2016). The *Fermi* LAT Collaboration does not report any statistically significant GeV emission from the bubble regions (Ackermann et al. 2017).

3.2. Spectral Analysis

The spectrum of the M31 disk, the bubbles, and the combined spatial model are shown in Figures 4 and 5. We summarize integral flux upper limits for the M31 disk, bubbles and combined models in Table 4 based on power-law fits (Equation (1)); the table also includes expected upper limits for the corresponding models. Figures 4 and 5 show quasi-differential limits calculated using the method described in Section 2. Plots based on the single power-law fits and tables giving the normalizations K for each fit are provided in the Appendix.

For the various single and joint fits, the limits on the VHE integral gamma-ray flux >1 TeV differ by roughly a factor of six when different spectral indices are assumed. We note that all upper limits are within the 95% intervals of the "expected" upper limits, defined using fits to background-only regions observed by HAWC (see Section 2). Thus the upper limits on the VHE flux are consistent with the expected sensitivity of the detector. For comparison, *VERITAS* upper limits corresponding to a large and a small test region of M31 (Bird 2016) are also shown in Figure 4.

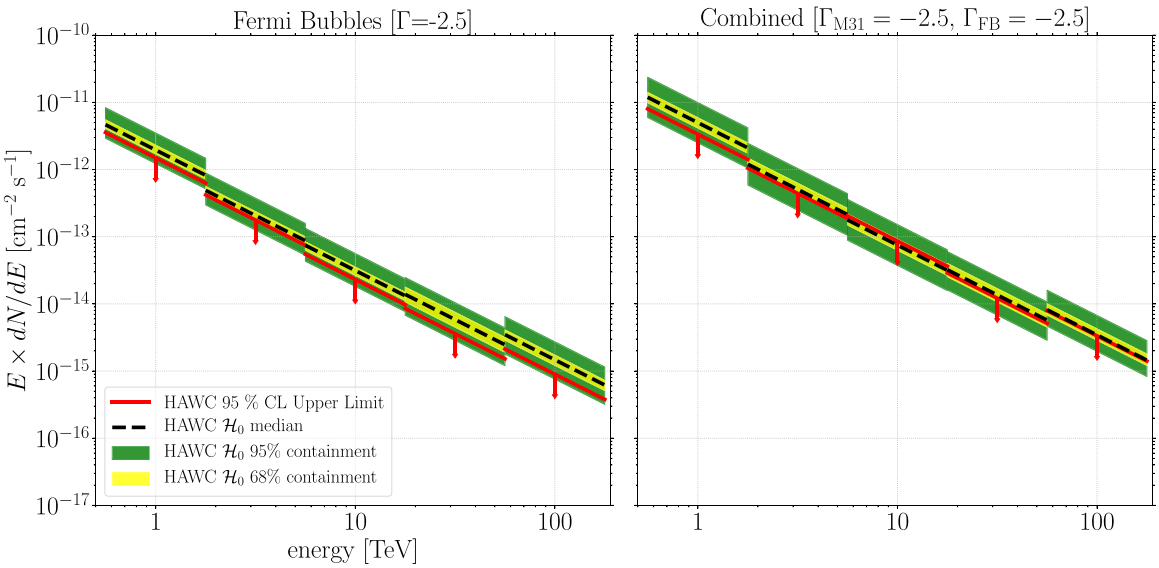

Figure 5. Left: 95% credible upper limits on VHE emission from FBs in M31, assuming an $E^{-2.5}$ spectrum. Right: 95% upper limits VHE emission from a joint fit of M31 and the FB regions, assuming independent spectral normalizations but the same power-law index of −2.5.

Table 4
Observed 95% Credible Upper Limits on the Emission from the M31 Galactic Disk and Its Bubbles

Model Template	Integral Flux Upper Limit (>1 TeV) (10^{-13} cm^{-2} s^{-1})	Expected Upper Limit (>1 TeV) (10^{-13} cm^{-2} s^{-1})
M31 disk ($\Gamma = -2.0$)	0.85	0.93 (0.77-1.09, 0.51-1.65)
M31 disk ($\Gamma = -2.5$)	3.75	3.83 (3.18-4.63, 2.08-6.03)
M31 disk ($\Gamma = -3.0$)	5.18	7.10 (6.00-8.77, 4.41-12.85)
FB ($\Gamma = -2.0$)	0.31	0.50 (0.39-0.63, 0.24-0.86)
FB ($\Gamma = -2.5$)	1.67	1.91 (1.62-2.27, 1.01-3.31)
FB ($\Gamma = -3.0$)	2.03	3.28 (2.86-4.03, 1.96-6.30)
Combined ($\Gamma_{M31} = -2.0$, $\Gamma_{FB} = -2.0$)	1.12	1.19 (0.97-1.48, 0.53-2.37)
Combined ($\Gamma_{M31} = -2.0$, $\Gamma_{FB} = -2.5$)	1.87	2.26 (1.78-3.03, 0.95-4.53)
Combined ($\Gamma_{M31} = -2.0$, $\Gamma_{FB} = -3.0$)	2.64	3.43 (2.63-4.88, 1.26-6.80)
Combined ($\Gamma_{M31} = -2.5$, $\Gamma_{FB} = -2.0$)	2.97	2.98 (2.30-4.17, 1.00-6.71)
Combined ($\Gamma_{M31} = -2.5$, $\Gamma_{FB} = -2.5$)	4.20	4.59 (3.75-5.84, 2.26-8.89)
Combined ($\Gamma_{M31} = -2.5$, $\Gamma_{FB} = -3.0$)	5.54	6.08 (4.83-7.40, 2.59-11.39)
Combined ($\Gamma_{M31} = -3.0$, $\Gamma_{FB} = -2.0$)	5.25	5.36 (4.24-6.57, 2.06-12.55)
Combined ($\Gamma_{M31} = -3.0$, $\Gamma_{FB} = -2.5$)	6.04	7.17 (5.44-8.77, 3.00-14.41)
Combined ($\Gamma_{M31} = -3.0$, $\Gamma_{FB} = -3.0$)	7.97	8.36 (6.99-10.19, 4.53-16.42)

Note. The expected median upper limits, as well as the 68% and 95% containment bands for the expected limits are given in the last column.

3.3. Cosmic-Ray Energy Density Interpretation

The calculated integral flux upper limits are used to infer the measured upper limits for the cosmic-ray energy density of the M31 disk above 1 TeV. The results are tabulated in Table 5 along with the uncertainties calculated by propagating the uncertainties in the disk mass and distance (see Table 3) and the systematic uncertainties on gamma-ray spectra measured with HAWC (Abeysekara et al. 2017a).

For the limits on the quasi-differential cosmic-ray energy density, we calculate $\omega_{\rm CR}(\geqslant 10E_\gamma)$ with E_γ set to the lower and higher end energy values for each energy bin in measured quasi-differential flux upper limits. As described in Section 2.2, $10E_\gamma$ is used as a proxy for the energy of the hadronic cosmic rays which produce gamma-rays via the production and decay of neutral pions. Then we use the values to compute the quasi-differential cosmic-ray energy density upper limits per energy bin using

$$\omega_{\rm CR}(10E_{\gamma,2} \geqslant 10E_\gamma \geqslant 10E_{\gamma,1}) = \omega_{\rm CR}(\geqslant 10E_{\gamma,1}) - \omega_{\rm CR}(\geqslant 10E_{\gamma,2}). \quad (5)$$

Table 5
Calculated Upper Limits on the Cosmic-Ray Energy Density for the M31 Disk for Three Spectral Indices

Model Template	Upper Limit $\omega_{\rm CR}$(>10 TeV) (eV cm^{-3})
M31 Disk ($\Gamma = -2.0$)	0.011 ± 0.009
M31 Disk ($\Gamma = -2.5$)	0.028 ± 0.022
M31 Disk ($\Gamma = -3.0$)	0.028 ± 0.022

As shown in Figure 6, our limits on the cosmic-ray energy density agree with the expected upper limits computed in

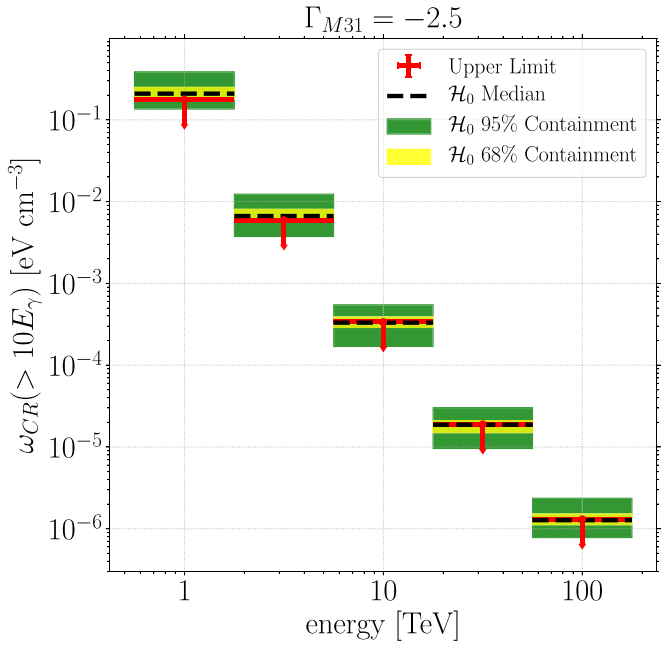

Figure 6. Upper limits on the energy density of cosmic rays in M31 > 10 TeV using the HAWC data set. The calculation assumes an $E^{-2.5}$ spectrum for the VHE gamma-rays.

background-only regions. Also, the cosmic-ray energy density upper limits for other spectral indices can be found in the Appendix, and also agree with the expected upper limits for background-only regions. For all energy bins considered in this work, the computed upper limits on ω_{CR} are higher than the average cosmic-ray energy density of the Milky Way calculated by the H.E.S.S. Collaboration (Abramowski et al. 2016), $\sim 10^{-3}$ eV cm^{-3}.

4. Conclusions

We have searched for gamma-ray emission from the nearby spiral galaxy, M31, applying spatial templates with 33 months of HAWC data. Independent and joint fits to the galactic disk and FB-like structures are performed. No significant emission is observed in the regions of M31 with the HAWC point source and extended source searches. Therefore, we report flux upper limits for the disk, the bubbles and the two features combined. The calculated integral flux upper limits are consistent with HAWC's sensitivity to background-only regions. The *Fermi* LAT spectral analysis of the M31 disk (Ackermann et al. 2017) provides a spectral index of Γ of -2.4 ± 0.1. When the spectrum is extrapolated under the assumption of no spectral break, the corresponding particle flux above 1 TeV has a value of 2.51×10^{-14} cm^{-2}s^{-1}. The flux upper limits from HAWC are about an order of magnitude higher than the extrapolated results, but consistent with the HAWC sensitivity. Our results do not coincide in energy range with *VERITAS* results (Bird 2016); however, our upper limits have an agreement with their upper limits.

Using the calculated flux upper limits of the M31 galactic disk, we estimate its cosmic-ray energy density using different fixed spectral indices at >1 TeV extrapolated to the full energy range of HAWC (see Table 5) as well as quasi-differential energy bins (Figure 6). We note that if we extrapolate the M31 disk spectrum measured by the *Fermi* LAT (Ackermann et al. 2017) to the 1–100 TeV range, we obtain an integral flux of 7.40×10^{-14} TeV cm^{-2} s^{-1}. This value can be interpreted as cosmic-ray energy density of 1.05×10^{-5} eV cm^{-3}, which is consistent with the upper limits on cosmic-ray energy density that we estimate with HAWC and report on in this work.

The HAWC limits can also be compared to the flux of the FBs in the Milky Way, normalized to the distance to M31, as described in Section 3.1. The upper limits of the integral flux of the M31 FB structures (0.30–2.68×10^{-13} cm^{-2}s^{-1}) are found to be higher than the extrapolated flux of 3.9×10^{-15} cm^{-2}s^{-1} by approximately two orders of magnitude.

This analysis is the first systematic study of the extended gamma-ray emission from the M31 region at TeV energies by a detector optimized to study extended emission. While no VHE gamma-rays from the disk of M31 or FB regions around the galactic nucleus were observed, we have constrained emission from this region up to 100 TeV. Future versions of this analysis will benefit from a factor of two increase in the size of the HAWC data set, as well as the development of high-resolution gamma-ray energy estimators in the HAWC reconstruction of gamma-ray air showers.

We acknowledge support from: the US National Science Foundation (NSF); the US Department of Energy Office of High-Energy Physics; the Laboratory Directed Research and Development (LDRD) program of Los Alamos National Laboratory; Consejo Nacional de Ciencia y Tecnología (CONACyT), México, grants 271051, 232656, 260378, 179588, 254964, 258865, 243290, 132197, A1-S-46288, A1-S-22784, cátedras 873, 1563, 341, 323, Red HAWC, México; DGAPA-UNAM grants AG100317, IN111315, IN111716-3, IN111419, IA102019, IN112218; VIEP-BUAP; PIFI 2012, 2013, PROFOCIE 2014, 2015; the University of Wisconsin Alumni Research Foundation; the Institute of Geophysics, Planetary Physics, and Signatures at Los Alamos National Laboratory; Polish Science Centre grant DEC-2018/31/B/ST9/01069, DEC-2017/27/B/ST9/02272; Coordinación de la Investigación Científica de la Universidad Michoacana; Royal Society—Newton Advanced Fellowship 180385. Thanks to Scott Delay, Luciano Díaz and Eduardo Murrieta for technical support.

Software: threeML/hawc-hal (https://github.com/threeML), AERIE-LiFF (https://github.com/rjlauer/aerie-liff, HAWC Collaboration).

Appendix
Results

Here, we present various spectral analyses carried out for different morphological models as mentioned in the main text. Figures 7 and 8 show the 95% (quasi-differential) upper limits and expected limits for the disk and bubbles combined with different spectral assumptions. Figure 9 shows the upper limits for the M31 disk only with different spectral assumptions and Figure 10 shows the upper limits for the bubbles only. Figures 11 and 12 are the quasi-differential upper limits for the disk only and bubbles only respectively. Table 6 has the fit results for all the fits with different spectral and morphological models considered. Finally, Figure 13 has the expected quasi-differential cosmic-ray energy density upper limits for different spectral indices produced using the computed gamma-ray upper limits.

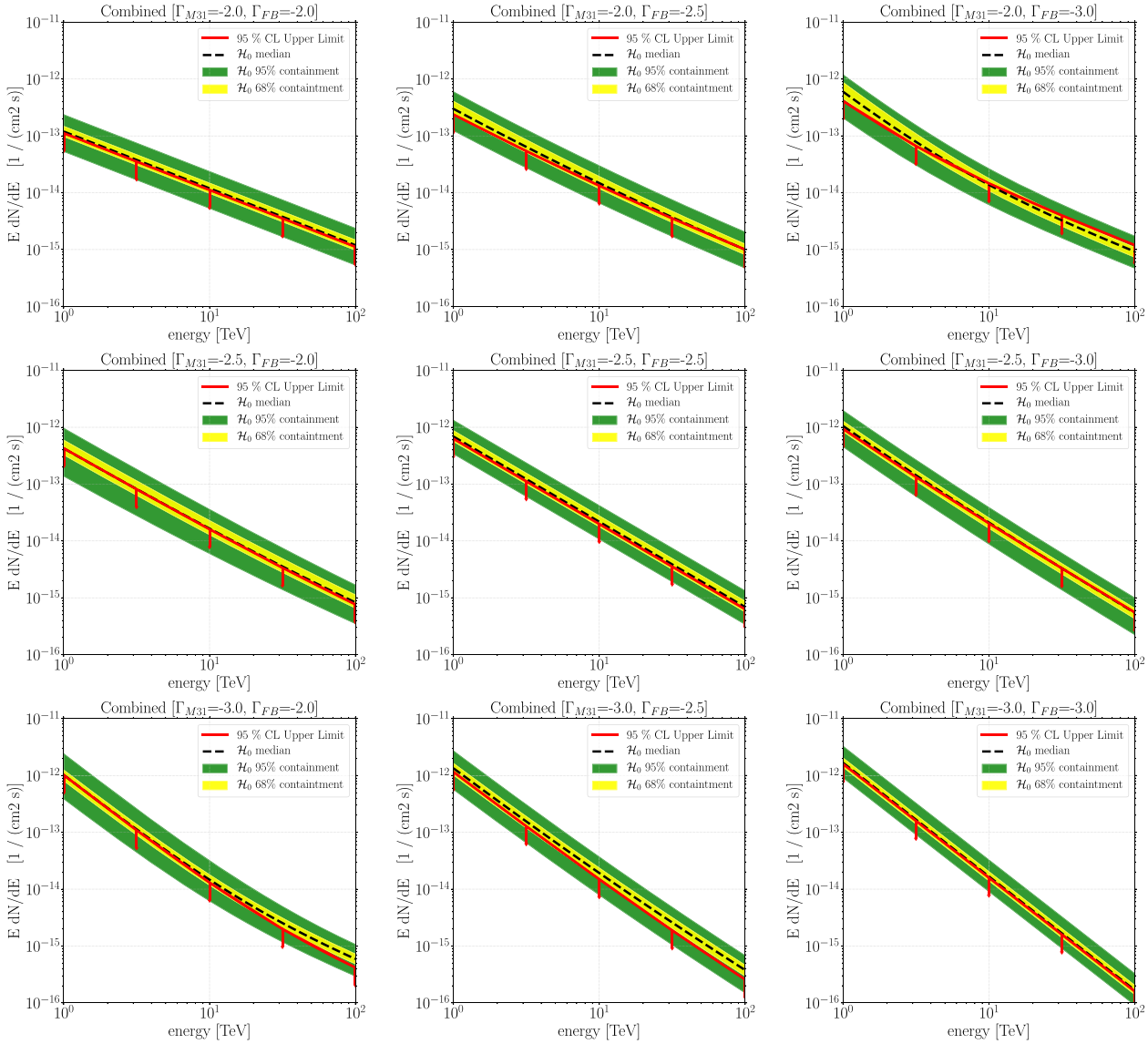

Figure 7. 95% credible interval upper intervals on the gamma-ray emission from the M31 disk and the M31 FBs, with nine combinations of spectral indices for the two regions.

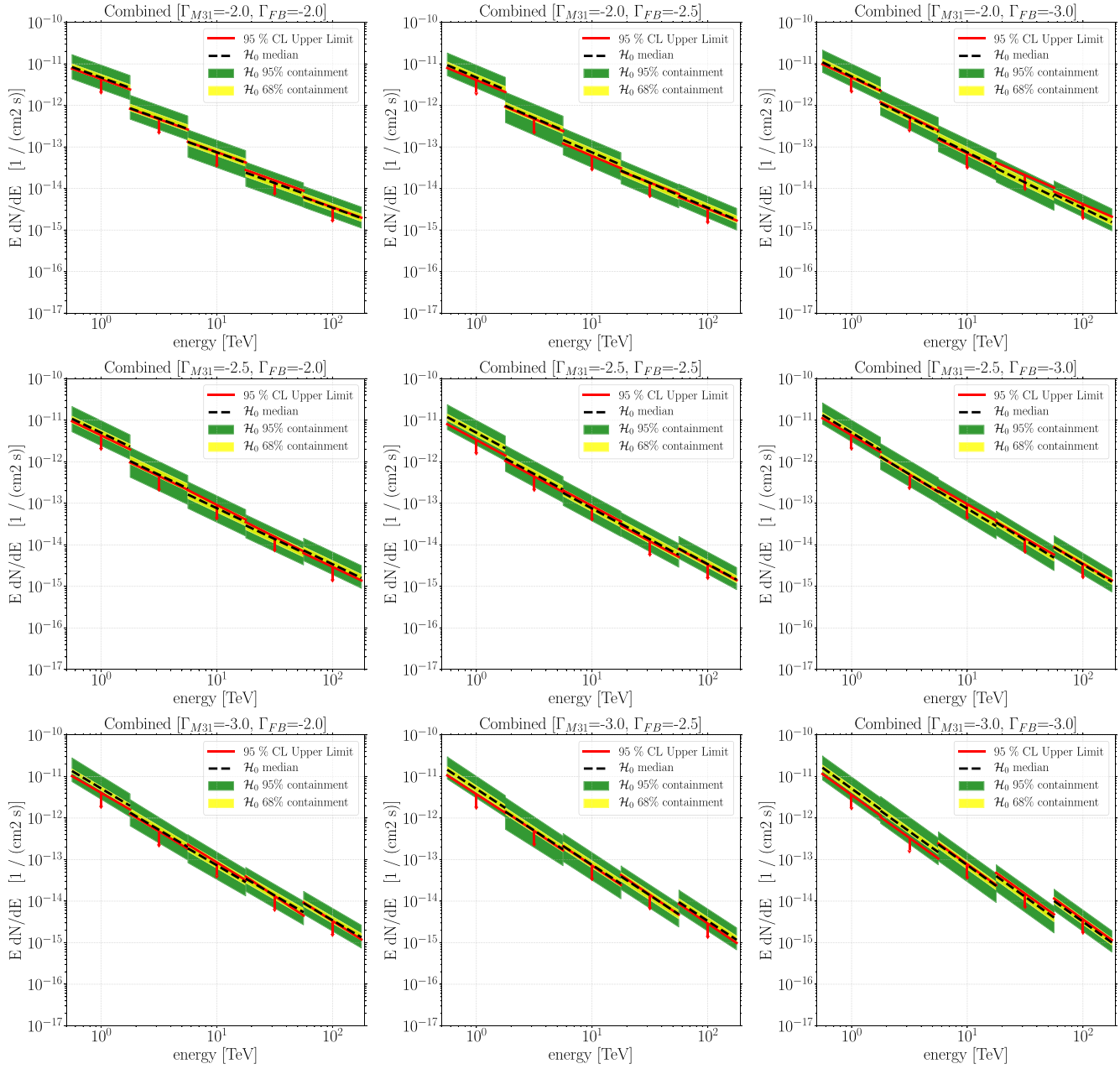

Figure 8. Measured quasi-differential upper limits and expected limits for the M31 disk and the FBs for different spectral index assumptions.

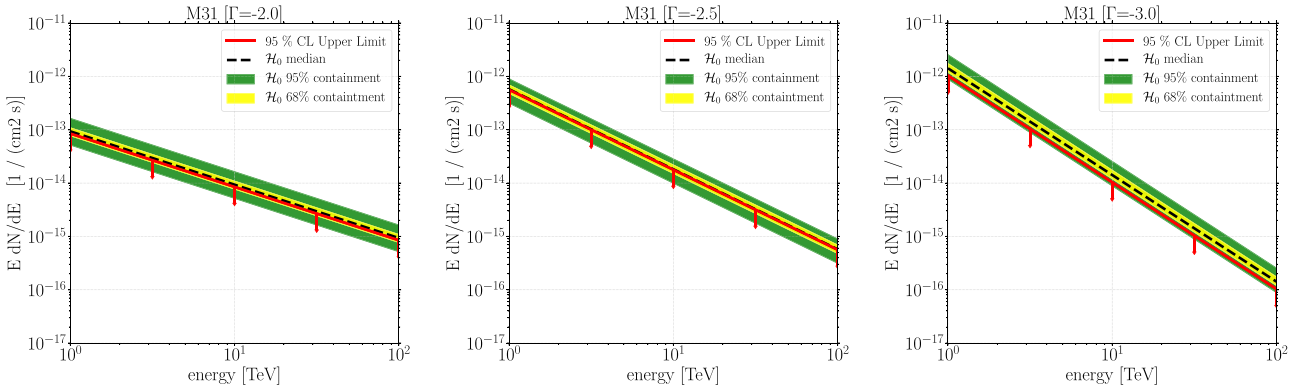

Figure 9. 95% credible interval upper intervals (and background-only expected upper limit bands) of the M31 disk assuming power-law emission with spectral index −2, −2.5, and −3. Dotted lines are the extrapolations of our upper limit for energies lower than HAWC's sensitivity.

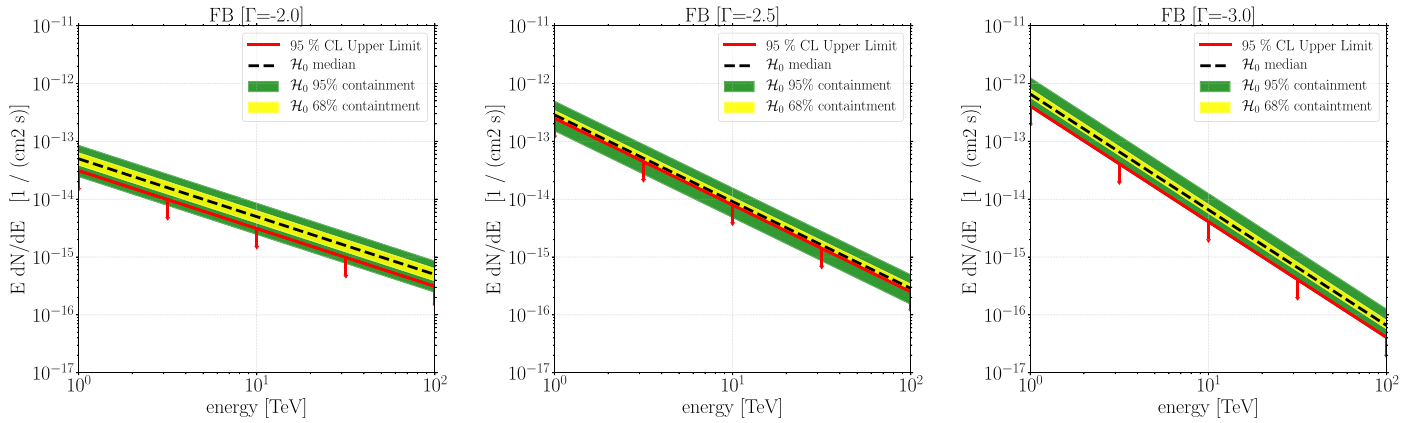

Figure 10. 95% credible interval upper limits and expected upper limits bands for the M31 "bubble" templates assuming a power law with spectral index −2, −2.5, and −3.

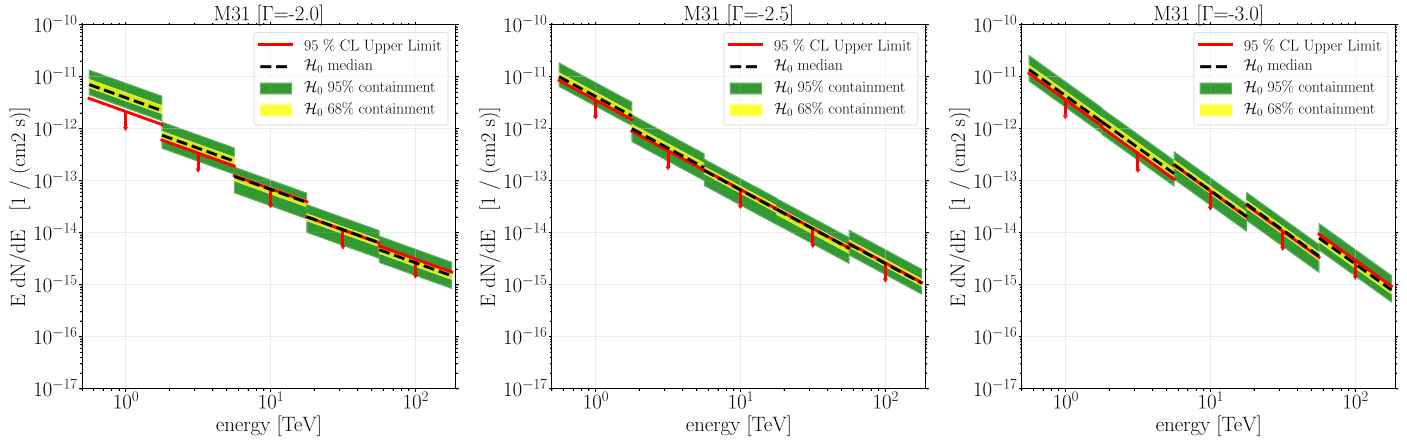

Figure 11. Measured quasi-differential upper limits and expected limits for the M31 disk for three assumed spectral indices.

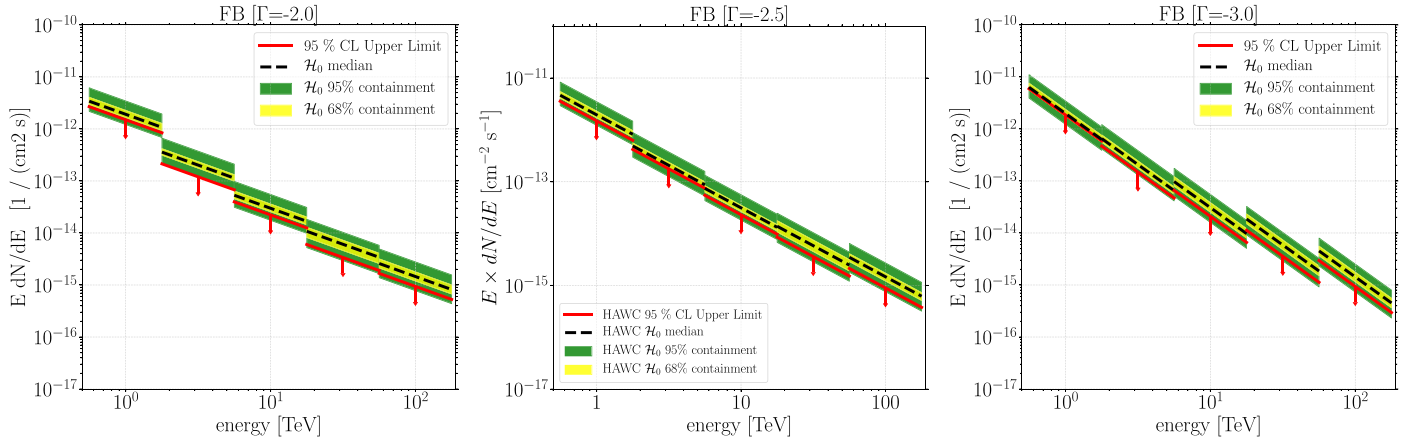

Figure 12. Measured quasi-differential upper limits and expected limits for the M31 FBs for three assumed spectral indices.

Table 6
Normalization Values for 95% Credible Interval Upper Limits, Expected Limits, and the Best Fit on the Emission from the M31 Galactic Disk and its Bubbles

Model Template	K (10^{-14} cm^{-2} s^{-1} TeV^{-1})	$K_{\rm expected}$ (10^{-14} cm^{-2} s^{-1} TeV^{-1})	$K_{\rm best\ fit}$ (10^{-14} cm^{-2} s^{-1} TeV^{-1})
M31 disk ($\Gamma = -2.0$)	8.50	9.34 (5.14–16.47, 7.69–10.94)	3.52 (2.63)
M31 disk ($\Gamma = -2.5$)	56.26	57.42 (31.27–90.48, 47.77–69.46)	21.76 (17.60)
M31 disk ($\Gamma = -3.0$)	103.59	141.91 (88.16–257.09, 119.96–175.46)	38.96 (32.44)

Table 6
(Continued)

Model Template	K (10^{-14} cm^{-2} s^{-1} TeV^{-1})	$K_{\rm expected}$ (10^{-14} cm^{-2} s^{-1} TeV^{-1})	$K_{\rm best\ fit}$ (10^{-14} cm^{-2} s^{-1} TeV^{-1})
FB ($\Gamma = -2.0$)	3.11	4.99 (2.45–8.57, 3.88–6.31)	1.06 (0.93)
FB ($\Gamma = -2.5$)	25.08	28.72 (15.15–49.65, 24.29–34.02)	7.19 (8.24)
FB ($\Gamma = -3.0$)	40.67	65.53 (39.17–126.04, 57.22–80.70)	14.73 (13.06)
Combined ($\Gamma_{M31} = -2.0$, $\Gamma_{\rm FB} = -2.0$)	7.80 3.38	7.49 (3.13–16.35, 6.24–9.09) 4.46 (2.17–7.39, 3.48–5.71)	2.84 1.12
Combined ($\Gamma_{M31} = -2.0$, $\Gamma_{\rm FB} = -2.5$)	8.46 15.36	7.76 (3.85–16.02, 6.41–9.41) 22.20 (8.53–44.00, 17.03–31.40)	3.38 4.73
Combined ($\Gamma_{M31} = -2.0$,$\Gamma_{\rm FB} = -3.0$)	11.67 29.49	8.70 (4.52–16.27, 6.93–10.16) 51.10 (16.09–103.44, 38.80–77.28)	4.60 9.65
Combined ($\Gamma_{M31} = -2.5$, $\Gamma_{\rm FB} = -2.0$)	39.00 3.73	38.07 (11.39–88.72, 29.03–53.68) 4.47 (2.36–7.98, 3.67–5.90)	13.34 1.31
Combined ($\Gamma_{M31} = -2.5$, $\Gamma_{\rm FB} = -2.5$)	46.96 16.03	44.23 (22.50–89.59, 36.67–55.52) 24.61 (11.43–43.72, 19.57–32.11)	15.98 5.69
Combined ($\Gamma_{M31} = -2.5$, $\Gamma_{\rm FB} = -3.0$)	51.07 42.67	48.77 (19.78–88.90, 38.29–58.56) 56.60 (25.44–109.20, 45.62–70.00)	19.56 16.89
Combined ($\Gamma_{M31} = -3.0$, $\Gamma_{\rm FB} = -2.0$)	98.67 3.18	97.25 (36.15–234.42, 76.61–119.26) 4.93 (2.57–8.34, 4.07–6.06)	26.26 1.22
Combined ($\Gamma_{M31} = -3.0$, $\Gamma_{\rm FB} = -2.5$)	99.92 15.71	107.32 (46.34–227.66, 80.12–131.09) 27.00 (10.29–45.41, 21.57–33.21)	38.04 5.09
Combined ($\Gamma_{M31} = -3.0$, $\Gamma_{\rm FB} = -3.0$)	110.85 48.55	109.35 (58.16–227.98, 91.45–132.16) 57.82 (32.36–100.36, 48.41–71.69)	36.28 18.41

Note. For the combined model results, 95% credible interval upper limits for M31 and FBs are given seperately.

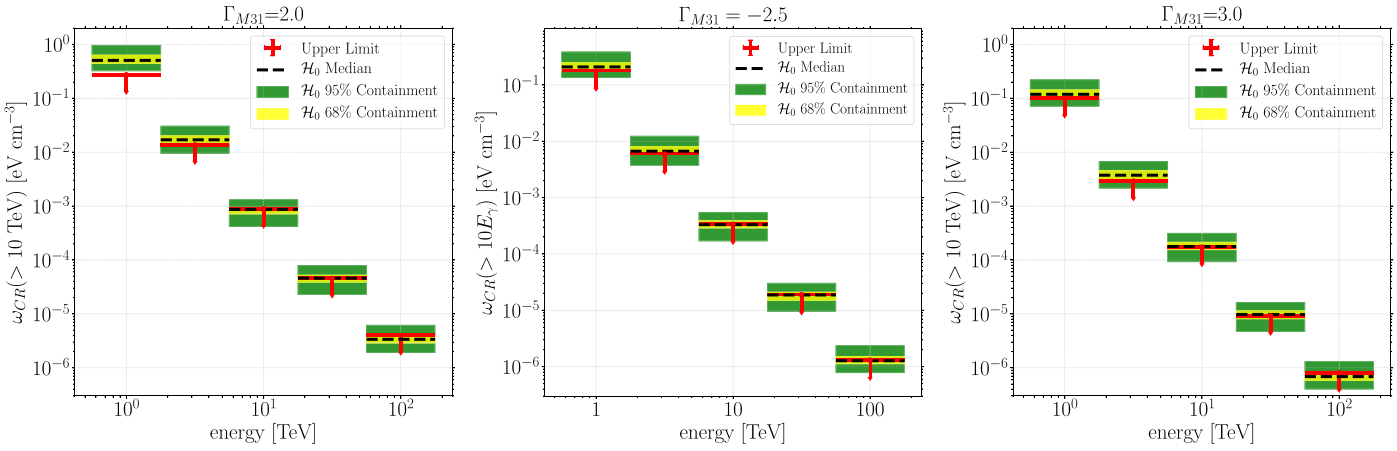

Figure 13. HAWC expected upper limits for cosmic-ray energy density for different spectral indices.

ORCID iDs

A. Albert https://orcid.org/0000-0003-0197-5646
J. A. García-González https://orcid.org/0000-0003-1327-0838
D. Kieda https://orcid.org/0000-0003-4785-0101
A. L. Longinotti https://orcid.org/0000-0001-8825-3624
K. Malone https://orcid.org/0000-0001-8088-400X
C. D. Rho https://orcid.org/0000-0002-6524-9769
D. Rosa-González https://orcid.org/0000-0003-1327-0838
T. Yapici https://orcid.org/0000-0002-5306-4804

References

Aartsen, M. G., Ackermann, M., Adams, J., et al. 2017, A&A, 607, A115
Abdo, A. A., Ackermann, M., Ajello, M, et al. 2010, A&A, 523, L2
Abeysekara, A. U., Albert, A., Alfaro, R., et al. 2017a, ApJ, 843, 39
Abeysekara, A. U., Albert, A., Alfaro, R., et al. 2017b, ApJ, 843, 40
Abeysekara, A. U., Albert, A., Alfaro, R., et al. 2019, ApJ, 881, 134
Abramowski, A., Aharonian, F., Benkhali, F., et al. 2016, Natur, 531, 476
Ackermann, M., Ajello, M., Albert, A., et al. 2017, ApJ, 836, 208
Ackermann, M., Albert, A., Atwood, W. B., et al. 2014, ApJ, 793, 64
Albert, A., Alfaro, R., Alvarez, C., et al. 2018, ApJ, 853, 154
Atkins, R., Benbow, W., Berley, D., et al. 2003, ApJ, 595, 803
Azimlu, M., Marciniak, R., & Barmb, P. 2011, AJ, 142, 139

Bird, R. 2016, ICRC (The Hague), 34, 851
Braun, R., Thilker, D. A., Walterbos, R. A. M., & Corbelli, E. 2009, ApJ, 695, 937
Dwek, E., & Krennrich, F. 2013, APh, 43, 112
Garmire, G., & Kraushaar, W. L. 1965, SSRv, 4, 123
Gorski, K. M., Hivon, E., Banday, A. J., et al. 2005, ApJ, 622, 759
Kang, Y., Bianchi, L., & Rey, S.-C. 2009, ApJ, 703, 614
Licquia, T. C., & Newman, J. A. 2015, ApJ, 806, 96
McConnachie, A. W., Irwin, M. J., Ferguson, A. M. N., et al. 2005, MNRAS, 356, 979
Miville-Deschenes, M.-A., & Lagache, G. 2005, ApJS, 157, 302
Nieten, C., Neininger, N., Guelin, M., et al. 2006, A&A, 453, 459
Pshirkov, M. S., Vasiliev, V. V., & Postnov, K. A. 2016, MNRAS, 459, L76
Sick, J., Courteau, S., Cuillandre, J.-C., et al. 2014, in IAU Symp. 311, Galaxy Masses as Constraints of Formation Models, ed. M. Cappellari & S. Courteau (Cambridge: Cambridge. Univ. Press), 82
Su, M., Slatyer, T. R., & Finkbeiner, D. P. 2010, ApJ, 724, 1044
Vianello, G., Lauer, R. J., Younk, P., et al. 2015, ICRC (The Hague), 34, 1042
Wilks, S. S. 1938, Ann. Math. Stat, 9, 60
Yin, J., Hou, J. L., Prantzos, N., et al. 2009, A&A, 505, 497
Yoast-Hull, T. M., Gallagher, J. S., & Zweibel, E. G. 2016, MNRAS, 457, L29
Younk, P. W., Lauer, R. J., Vianello, G., et al. 2015, ICRC (The Hague), 34, 948